Heat flow of the Mozambique channel: New data and predicted surface heat flow map

Eloïse Bessière, Jeffrey Poort, Tristan Cornu, Sylvie Leroy

Marine and Petroleum Geology 162 (2024) 106723

Contents lists available at ScienceDirect

Marine and Petroleum Geology

journal homepage: www.elsevier.com/locate/marpetgeo

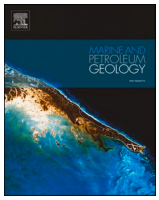

Heat flow of the Mozambique channel: New data and predicted surface heat flow map

Eloïse Bessière [a,b,*], Jeffrey Poort [a], Tristan Cornu [c], Sylvie Leroy [a]

[a] Sorbonne Université, CNRS-INSU, Institut des Sciences de la Terre Paris, ISTeP UMR, 7193, 4 Place Jussieu, F-75005, Paris, France
[b] Now at Université Côte d'Azur, CNRS, Observatoire de la Côte d'Azur, IRD, Géoazur, UMR, 7329, 250 Rue Albert Einstein, Sophia Antipolis, 06560, Valbonne, France
[c] TotalEnergies, 1201 Louisiana Street, Houston, TX, 77002, USA

A B S T R A C T

The Mozambique Channel, a complex domain composed of passive margins and oceanic crust affected by younger strike-slip and volcanic activity, is still poorly studied for surface heat flow. We present 33 new marine-type heat flow estimations acquired offshore in 2014–2015 during the MOZ cruises, completed with 4 new heat flow values derived from reappraised old well sites (PAMELA project). Offshore heat flow is generally low to normal and does not display strong variations. As poor data coverage persists in large parts of the area, we performed a heat flow prediction mapping using the similarity method. Based on an extrapolation of old and new data guided by 14 geological and geophysical proxies, we obtain on a 0.1° × 0.1° grid a predicted heat flow and its uncertainty from the statistics of all values at global grid points with similar proxies. We succeeded to obtain good predictability on 70% of pixels and an RMS error <2.3 mW/m^2. The proxies selected for the prediction include a map of genetic domains, sediment thickness, topography and bathymetry, crustal ages, Curie point depth, Free air anomaly, distances to volcanoes, tectonic structures and continent-ocean boundaries. The new Mozambique heat flow map shows a predominantly low offshore heat flow of around 50 mW/m^2, associated with the Jurassic and early Cretaceous age of the oceanic crust. Several heat flow anomalies standoff to this background heat flow with two main orientations: low heat flow anomalies with a N–S orientation and high anomalies with a mostly NE-SW orientation, which are linked mainly to tectonic structures.

1. Introduction

The surface heat flow is a crucial parameter in many topics, like geothermal exploration, crustal structure nature, margin evolution or Earth dynamics (Davies, 1989; Furlong et al., 1995; Fuchs et al., 2023; Korenaga, 2008; Loyd et al., 2007; Muffler and Cataldi, 1978). The Earth's coverage of heat flow is extremely heterogeneous and relatively poor in several areas, especially offshore. Yet, the number of acquired values is constantly increasing (Benfield, 1939; Bullard, 1939; Fuchs et al., 2021; Lee and Uyeda, 1965; Pollack et al., 1993). Some authors succeeded to complete this database with additional data from confidential oil exploration studies (e.g. Lucazeau, 2019). Heat flow data from boreholes and from marine probe instruments are obtained in very different depth intervals and are dealing with different types of perturbations from surface processes, but if proper corrections are applied both can be considered as an appropriate estimate of the amount of thermal energy that the Earth loses per unit surface area and time. In order to better constrain the heat flow coverage and evolution, several indirect approaches have been developed and published as well. Indeed, heat flow can be derived from the depth of the Bottom Simulating Reflectors (BSR) identified along high-resolution seismic profiles (Grevemeyer and Villinger, 2001; Hyndman et al., 1992; Yamano et al., 1982) or from the Curie Point Depth (Li et al., 2017). Using extrapolation and predictive approaches, authors have tried to get a global full-coverage image of the heat flow. Commonly, extrapolation and predictive approaches are based on geology (Lee and Uyeda, 1965), oceanic and/or continental crust age (Artemieva, 2006; Davies, 2013; Sclater, 1977), or again upper mantle shear velocities (Shapiro and Ritzwoller, 2004). Goutorbe et al. (2011) published a more integrating process using the stacking of a large number of geologic or geophysical proxies in order to get relevant information for better constraining the heat flow predictions. The predictive global mapping is computed with a purely statistical calculation: the similarity method (Lucazeau, 2019). This method is based on the evaluation at each grid location of the number of similarities with several heat flow proxies at all other locations of the grid where heat flow is known. Due to the improvement of acquisition techniques and signal treatments, geologic and geophysical global databases are constantly increasing in number, quality and resolution. The method was initially applied on a 1° × 1° global grid (Goutorbe et al., 2011), but it was recently upgraded to a 0.5° × 0.5° global prediction by Lucazeau (2019).

In this study we propose to apply the similarity method to a regional

* Corresponding author. Sorbonne Université, CNRS-INSU, Institut des Sciences de la Terre Paris, ISTeP UMR, 7193, 4 Place Jussieu, F-75005, Paris, France.
E-mail addresses: eloise.bessiere@gmail.com, eloise.bessiere@geoazur.unice.fr (E. Bessière).

https://doi.org/10.1016/j.marpetgeo.2024.106723
Received 10 May 2023; Received in revised form 18 January 2024; Accepted 19 January 2024
Available online 20 January 2024

area with an increased resolution of 0.1° × 0.1° grid. We choose as a study area a divergent-transform continental margin, i.e., the Mozambique Channel (Fig. 1) where we collected several new heat flow data. This type of margin is often characterized by a narrow necking zone, steep continental slopes, marginal plateaus systematically located between the platform and the lower continental slope, occasionally marginal ridges located at the edge of the continental slope and some specific sedimentary processes. Such geological and tectonic structure implies a complex thermal evolution. The study area is still poorly constrained by heat flow determination (Fig. 2), but several recent campaigns of heat flow acquisition and re-appraisal succeeded to upgrade the local database. Thus, this work will detail these new data acquisitions as well as a predictive mapping of the heat flow variation on the Mozambique Channel area (Figs. 1 and 2). A good knowledge of the present-day surface heat flow helps to better constrain the thermal state and are a vital parameter in any modeling study of the basin evolution and regional tectonic activity.

2. Geological and geodynamic settings

The Mozambique passive margin, located between Africa and Madagascar island, is thus located between Archean and Paleoproterozoic cratons which have been affected by several orogenic systems (Fig. 1; Cawood and Buchan, 2007; Collins and Pisarevsky, 2005; Jacobs and Thomas, 2004; Ring et al., 2002). From the Paleoproterozoic to the Neoproterozoic, these several collisional episodes contributed to the development of NE/SW-NW/SE crustal-scale structures associated to a continental block amalgamation (Castaing, 1991; Daly et al., 1989; Daszinnies et al., 2009; Jacobs et al., 2008; Macgregor, 2018; Riedel et al., 2013) and the Mozambican belt formation (Bingen et al., 2009; Jacobs et al., 2008). Following these orogenic phases, a continental rifting episode, the Karoo rifting, occurred from the Carboniferous to the Late Jurassic between Africa and Antarctica, reactivating the orogenic-inherited structures into extensional trends and dismembering the Gondwana supercontinent (Fig. 1; Castaing, 1991; Catuneanu et al., 2005; Cox, 1992; Mahanjane, 2012; Reeves, 2018; Watkeys, 2002). Thus, the development of large intracratonic basins allowed the deposit of Upper Carboniferous to Lower Jurassic sediments. The Early to Middle Jurassic period is marked by the emplacement of a large igneous province (LIP) around 180 Ma, named the Karoo-Ferrar igneous province, respectively located on both the South-Eastern Africa and the Eastern Antarctica (Cox, 1992; Ivanov et al., 2017; Klausen, 2009; Melluso et al., 2008; Riley et al., 2003, 2020). Whatever the cause and the precise timing of this event, such

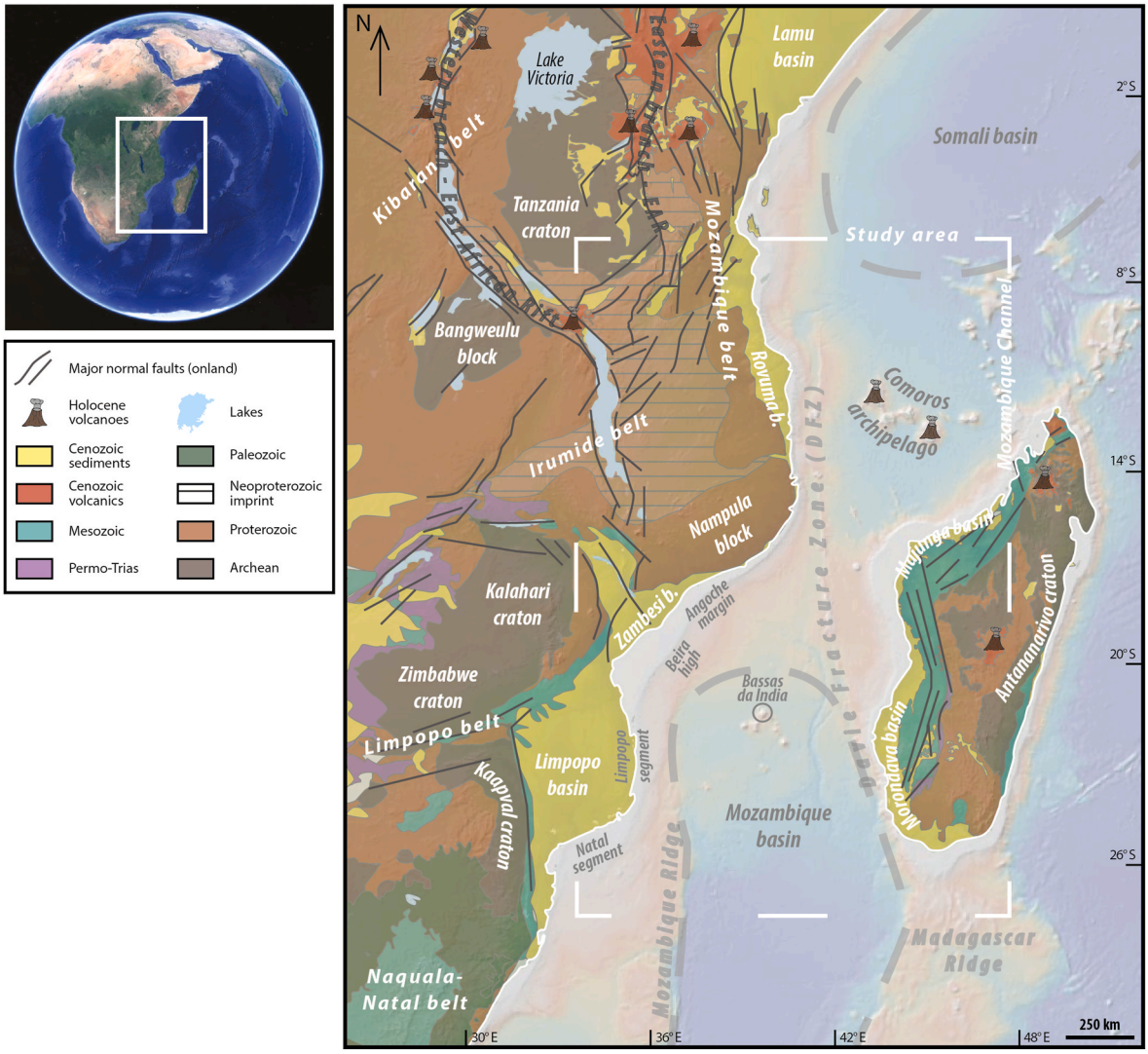

Fig. 1. Regional map of the interest zone: the Mozambique Channel. The map synthetizes the main geological provinces, i.e., the Archean cratons, the Proterozoic belts, the Cenozoic basins, and the major tectonic structures affecting the continental part of the study area. The bathymetry, the two major offshore basins and the main localities are also presented.

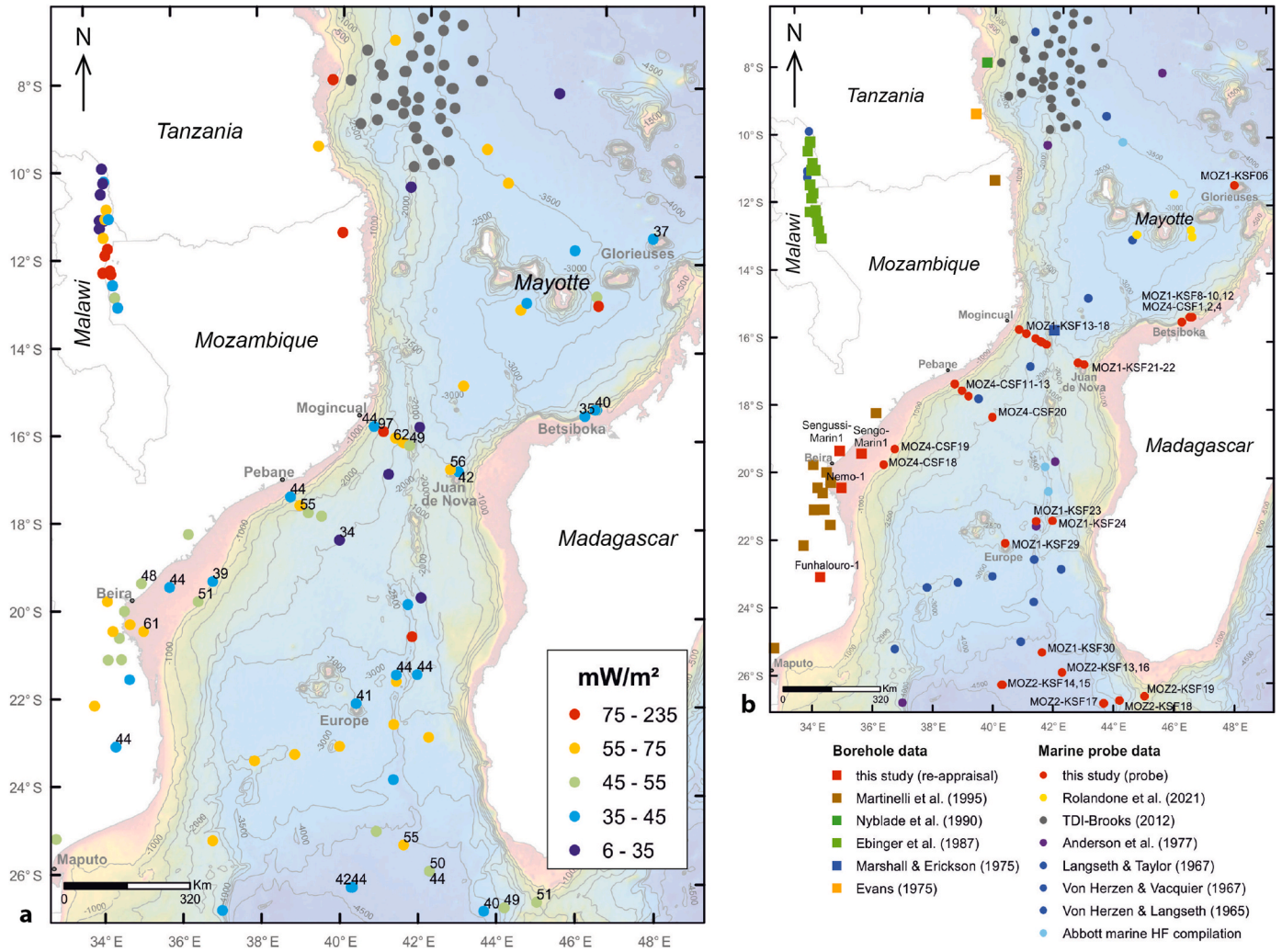

Fig. 2. Presentation of the heat flow data available in the Mozambique Channel area. (a) Detail of the heat flow measurements when they are not confidential, the dot color is related to the heat flow value, i.e., cold colors highlight low heat flow values, while hot colors are related to high heat flow values. Numbers close to dots are heat flow values for the new acquisitions. Grey dots are confidential data. See the data section for data description (b) Presentation of the heat flow measurements according to the acquisition type and the publications. Squares are related to borehole data while dots are related to marine-type measurements.

large amount of volcanism impacted the rifting evolution by playing a role in the lithosphere rheology or in the localization of the deformation (Ivanov et al., 2017; Storey, 1995). Because the breakup age is not precisely constrained, from ~166 to ~156 Ma, as well as the age of the first oceanic crust, from ~157 to ~127 Ma (Gaina et al., 2013; Jokat et al., 2003; Leinweber et al., 2013; Moulin et al., 2020; Mueller et al., 2016; Segoufin, 1978; Senkans et al., 2019), the first post-rift sediments are estimated to be Middle to Late Jurassic (Leinweber et al., 2013; Senkans et al., 2019).

At present, the Mozambique Channel is mainly characterized by continental and oceanic crusts intermediate domains such as extended continental crust, magmatic or volcanic crusts (Fig. 1). Even if the precise geometry of these domains remains a matter of debate, the overall characterization is quite well-constrained.

During Middle Jurassic to Cretaceous, the Madagascar craton is drifted due to the N–S oceanic spreading (Coffin and Rabinowitz, 1987; Franke et al., 2015; Reeves, 2014; Storey et al., 1995) which is responsible for the development of transpressional structures (Fig. 1). From the Kenya to the South of Madagascar, the oriented-N-S Davie Fracture Zone (DFZ) marks the separation in the Mozambique Channel between the Comoros Basin in the north of Madagascar and the Mozambique Basin located in the west of Madagascar (Fig. 1).

The continental domain is affected by several low-angle normal faults, almost showing a N–S trend and generally gently dipping toward the ocean (Watremez et al., 2021, Fig. 3). Locally, strike-slip component is suspected due to the observation of a negative flower-structure geometry (Roche et al., 2021). The transitional or thinned continental domain is also affected by N–S faults, delimitated by major strike-slip faults and often associated with SDRs formation (Roche et al., 2021, Fig. 3). The oceanic domain highlights various fault types, i.e., low-to high-angle normal faults, reverse faults and strike-slip faults (Watremez et al., 2021). Several segments, i.e., geographical subdivisions, are bounded by NE-SW transfer zones (Fig. 3; e.g., Senkans et al., 2019). The Beira High and the Angoche segments show an oblique orientation of normal faults becoming NE-SW instead of N–S in the rest of the area (Senkans et al., 2019; Roche et al., 2021, Figs. 1 and 3).

3. Heat flow data: methods and results

3.1. Previous data

Based on the New Global Heat Flow (NGHF) database (Lucazeau, 2019), 35 heat flow data are available in the Mozambique Channel (Fig. 2). Heat flow acquired in 12 boreholes on the Mozambique shore and shelf (mostly near the Limpopo segment) have been described by Martinelli et al. (1995) (Fig. 2). For the offshore Mozambique Channel

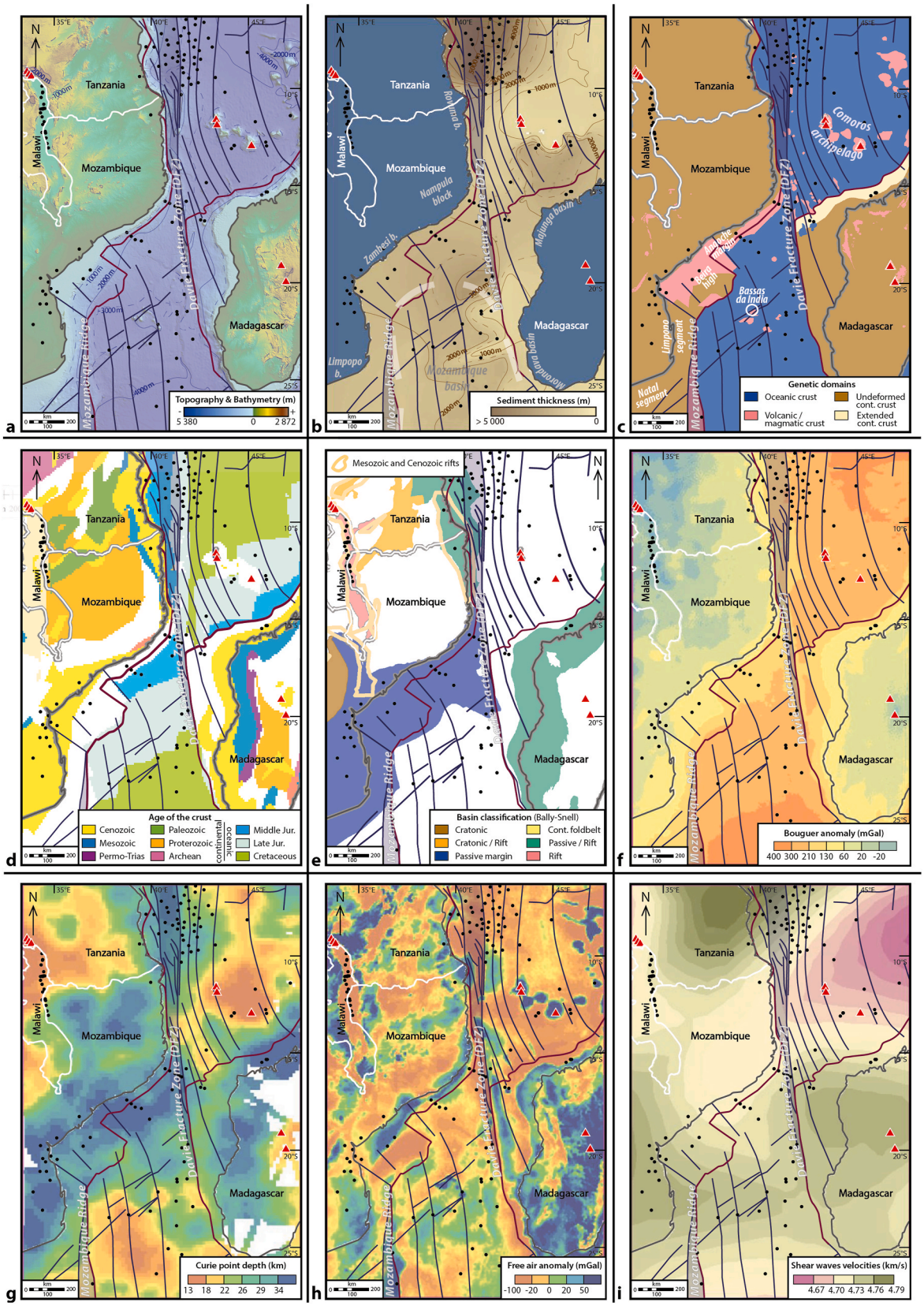

Fig. 3. Cataloging of all the proxies used in the heat flow calculation for the Mozambique Channel. (a) Map of the bathymetry and topography (Gebco2020). (b) Map of the sediment thickness (GlobSed; Straume et al., 2019). (c) Map of the genetic domains. (d) Map of the continent/ocean crust age classification. (e) Map of the basin classification (Bally-Snell) and of the Mesozoic and Cenozoic rifts. (f) Map of the Bouguer anomalies (BGI; Bonvalot et al., 2012). (g) Map of the Curie point depth (Li et al., 2017). (h) Map of the free air anomalies (BGI; Bonvalot et al., 2012). (i) Map of the mantle anisotropy. Commonly to all maps, the dark blue lines show the major tectonic features, the Continent-Ocean Boundaries are drawn with purple line, the red triangles show the location of the Holocene volcanoes and heat flow data are located by black dots.

area, heat flow was measured in DSDP (Figs. 2), 242 boreholes in 1972 (Marshall and Erickson, 1974) and 18 heat flow probe data were acquired between 1965 and 1977 (Abbott compilation; Anderson et al., 1977; Langseth and Taylor, 1967; Von Herzen and Langseth, 1965). Four more probe determination were recently obtained near Mayotte Island (Fig. 2; Rolandone et al., 2022). These data show an overall low heat flow for the whole Mozambique Channel (52 ± 14 mW/m^2, excluding two extremely high values). The lowest (29–30 mW/m^2) and highest (106–240 mW/m^2) heat flow values are both found on or near the DFZ. One isolated high heat flow value was recently also measured east of Mayotte near Fani Maoré, an active underwater volcano (Masquelet et al., 2022; Rolandone et al., 2022; Thinon et al., 2022).

In the map of Fig. 2 we also included data north of the channel, in the southern part of the Somali basin (Abbott compilation and confidential data; Anderson et al., 1977; Evans, 1975; Nyblade et al., 1990; Von Herzen and Langseth, 1965) and on-land at the lake Malawi rift (Ebinger et al., 1987; Von Herzen and Vacquier, 1967). The Somali basin data is quite similar to the Mozambique channel (55 ± 11 mW/m^2), while the Malawi rift shows a much higher variability, with values between as low as 6 mW/m^2 and as high as 172 mW/m^2 (56 ± 45 mW/m^2).

3.2. New data acquisition

New heat flow data have been acquired during the PAMELA Project (Fig. 2) by (1) the re-appraisal of old well data from the oil industry, and (2) by the acquisition of new offshore heat flow data during three oceanographic cruises (MOZ1, MOZ2 and MOZ4; Jouet and Deville, 2015; Olu, 2014; Robin and Droz, 2014). These new data are focused on the Angoche margin, the Beira High and Limpopo margin, the Mozambique basin and the Betsiboka seepage area (Figs. 1 and 2).

3.2.1. Borehole re-appraisal data

Four borehole heat flow assessments were obtained (Fig. 2; Vincent, 2016) from old corrected BHT data and as well as new thermal conductivity estimation based on the well log data using the neural network method of Goutorbe et al. (2008) (Tables 1 and S1). The BHT estimates are obtained in the sedimentary column at different depth levels between 530-1197 m and 3170–4220 m. The thermal gradient obtained from a linear regression is strongly averaged over a large depth interval and are deep enough not to be strongly affected by paleoclimate or other surface perturbations. Three of them are closely located, two in the Beira High segment, and the other in the Limpopo segment, while the last one is located more to the South in the Natal segment. Thus, a thermal/-seismic profile in the Beira High can be studied.

3.2.2. Marine-type probe data

Offshore, thirty-three marine-type heat flow data (Fig. 2 and Table 2) were obtained using autonomous high-precision temperature sensors attached to piston cores that allowed in-situ measurements of temperatures and thermal gradients within sediments (Fig. S1). The thermal conductivities were measured on board on the recovered sediment cores. No correction for in-situ pressure or temperature was applied for these near-surface sediments.

The THP temperature sensors (NKE©) have an accuracy of 0.005 °C and a resolution of 0.001 °C. Depending on the piston core length (10 or 20 m) and operational constraints, the amount of attached sensors (5 or 6) as well as the distance between them has been variable (Fig. S1). All the different configurations are detailed in Table 2 and Fig. S2. This device is completed by an inclinometer at the top of the piston core to allow the record of the piston core verticality within sediments (Table 2). The device is left in the sediments for 7–10 min to log the temperatures at the different sensors, and equilibrium in-situ temperatures were calculated using the extrapolation method described by Bullard (1954). The resulting temperature-depth profiles are near linear at subsurface depths of more than 2 m, highlighting stable thermal conditions at the measured depth intervals (Table 2 and Table S2). The thermal gradients at each station were obtained through linear regression and varied from 39 to 98 mK/m (average of 51 ± 12 mK/m).

The thermal conductivity measurements onboard were made using the TPSYS02/TP08 device (Hukseflux©) which applies the continuous heating needle probe method (Von Herzen and Maxwell, 1959). Measurements were made through a small hole on closed cores immediately after recovery and have therefore temperature and saturation conditions close to in-situ. Measurements were made along the whole length of the sediment core at an interval spacing of 50 or 100 cm. A total of 522 measuring points were realized on the 33 cores stations (Table 2 and Table S3). The thermal conductivity values at all measured intervals are ranging from 0.78 to 1.66 W/m/K, but the harmonic mean at the different stations is very stable: 0.96 ± 0.05 W/m/K.

Heat flow values have been calculated using the mean thermal gradient determined by linear regression and the harmonic mean or constant thermal conductivity, all the new data are summarized in Table 2. Note that the heat flow value for station MOZ1-KSF06 was previously published by Rolandone et al. (2022), but these authors did not give any details on the heat flow acquisition or the measurement quality.

3.3. Heat flow data

The 33 new marine probe data and the 4 borehole re-appraisal data result in an average heat flow of 49 ± 11 mW/m^2. Most of the new values range between 35 and 66 mW/m^2, but one station on the Mogincual margin and not far from the DFZ reached 97 mW/m^2 (Fig. 2). Two short heat flow profiles on the Mozambique margin (off Mogincual and Pebane) show both a local heat flow increase at the ocean-continent transition more than +10 mW/m^2 from a base heat flow of 34–44 mW/m^2 (Figs. 2 and 3). East of the Beira High, the 4 new borehole data and two probe data indicate a heat flow of 39–46 mW/m^2 with one exception of 61 mW/m^2 in the Nemo-1 borehole (Fig. 2). South-East of Madagascar, in and around the Zambesi channel, heat flow is increased slightly with values ranging 40–55 mW/m^2 (Fig. 2). North-West of Madagascar, in the Majunga basin, a heat flow of 40–66 mW/m^2 is obtained in the Betsiboka offshore area affected by gas seepage (Fig. 2). A relatively low background heat flow of 37 mW/m^2 has been obtained more North close the Glorieuses seamount (Fig. 2).

Table 1
Synthesis of the four borehole re-appraisal data (BHT) according to Vincent (2016). The thermal conductivity was estimated from log data from Funhaloura-1 well based on the neural network method of Goutorbe et al. (2008). The same conductivity was applied in the others nearby wells (noted with *) because of similar stratigraphic compositions.

Well name	Longitude	Latitude	Depth upper BHT (m)	Depth lower BHT (m)	Number of BHTs	Thermal gradient (mK/m)	Thermal conductivity (W/m/K)	Heat flow (mW/m^2)
Funhalouro-1	34.4166	−23.1394	530	4167	5	18.4	2.44	44.9
Nemo-1	35.1814	−20.512	1061	4091	5	25.1	2.44*	61.3
Sengo-Marin-1	35.8308	−19.5139	1197	4227	3	18.1	2.44*	44.7
Sangussi-Marin-1	35.1512	−19.4121	750	3170	2	19.9	2.44*	48.5

Table 2
Synthesis of the thermal measurements associated with acquisition details for the MOZ1, MOZ2 and MOZ4 cruises.

Cruise name	Site name	Longitude	Latitude	Date	tilt	Zmax	N	Thermal gradient		Thermal conductivity		Heat flow	
					(°)	(m)		mean (mK/m)	error (mK/m)	mean (W/m/K)	error (W/m/K)	mean (mW/m^2)	error (mW/m^2)
MOZ1	KSF06	47.185	−11.44	September 30, 2014		7.8	5	38.8	2.1	0.968	0.061	37.6	4.4
MOZ1	KSF08	45.987	−15.368	October 04, 2014		12.2	5	42.1	0.2	0.930	0.042	39.1	1.9
MOZ1	KSF09	45.956	−15.361	October 05, 2014	3.7	8.5	5	41.2	0.2	0.905	0.019	37.3	0.9
MOZ1	KSF10	45.716	−15.519	October 07, 2014	5	9.5	5	39.9	1.1	0.887	0.034	35.4	2.3
MOZ1	KSF12	45.96	−15.364	October 08, 2014	4.7	8.5	5	64.4	0.2	0.938	0.021	60.5	1.5
MOZ1	KSF13	41.408	−16.185	October 10, 2014	5.4	6.5	6	62.8	3.5	0.851	0.034	53.5	5.1
MOZ1	KSF14	40.744	−15.836	October 10, 2014	4.5	8.4	6	46.3	2.6	0.962	0.037	44.5	4
MOZ1	KSF15	40.968	−15.956	October 10, 2014	8.3	4	3	96.9	2.7	1.000	0.072	96.9	9.6
MOZ1	KSF16	41.247	−16.101	November 11, 2014	5.3	7.3	6	58.7	1.8	0.951	0.110	55.8	10.7
MOZ1	KSF17	41.448	−16.206	November 11, 2014	6	9.1	6	71.2	0.7	0.876	0.026	62.4	2.5
MOZ1	KSF18	41.586	−16.277	November 11, 2014	3.2	5.3	5	51.9	2.5	0.949	0.022	49.3	3.5
MOZ1	KSF21	42.758	−16.847	November 12, 2014	4.2	8.4	6	43.4	1.2	0.963	0.035	41.8	2.7
MOZ1	KSF22	42.567	−16.802	November 13, 2014	5.2	7.5	6	57.9	1.8	0.963	0.028	56	3.4
MOZ1	KSF23	41.346	−21.53	November 16, 2014		11.8	6	47.3	2	0.941	0.030	44.5	3.3
MOZ1	KSF24	41.861	−21.518	November 17, 2014		8.8	6	46.5	2.5	0.959	0.057	44.6	5.1
MOZ1	KSF29	40.368	−22.198	November 22, 2014		12	5	42.7	3.1	0.987	0.027	42.2	4.6
MOZ1	KSF30	41.595	−25.427	November 24, 2014		8.7	5	57.5	1.2	0.965	0.030	55.5	2.9
MOZ1	KSF13	42.2746	−26.008	November 24, 2014		12.5	5	42.7	4.1	1.034	0.093	44.1	8.2
MOZ	KSF14	40.288	−26.4115	November 27, 2014		7.6	5	42.8	2.6	1	0.01	42.8	3
MOZ2	KSF15	40.288	−26.4115	November 27, 2014		12.5	5	44.7	1.8	0.990	0.072	44.2	5
MOZ2	KSF16	42.2746	−26.008	November 28, 2014		12.8	5	50.4	0.8	1.008	0.084	50.8	5
MOZ2	KSF17	43.6803	−26.887	November 29, 2014		9.7	5	44.6	2.6	0.915	0.041	40.9	4.2
MOZ2	KSF18	44.1969	−26.7889	November 30, 2014		10.5	5	51.3	2.2	0.962	0.025	49.4	3.4
MOZ2	KSF19	45.0133	−26.6298	November 30, 2014		8.3	5	53.8	2.1	0.940	0.042	50.6	4.3
MOZ2	CSF01	45.9605	−15.3636	November 15, 2015		9.9	5	65.5	0.1	1.006	0.034	66	2.3
MOZ4	CSF02	45.9564	−15.3615	November 15, 2015		11.2	5	48.7	1.7	0.989	0.037	48.1	3.5
MOZ4	CSF04	45.9518	−15.3705	November 17, 2015		10.4	4	43.0	4.7	0.945	0.055	40.6	6.8
MOZ4	CSF11	39.1865	−17.825	November 20, 2015	0.5	11.2	6	44.4	0.5	1.019	0.048	45.3	2.6
MOZ4	CSF12	38.9834	−17.6552	November 21, 2015	1	11.5	6	52.7	1.9	1.058	0.067	55.8	5.5
MOZ4	CSF13	38.7545	−17.4639	November 24, 2015	1.3	19.2	5	43.2	3	1.018	0.130	44	8.7
MOZ4	CSF18	36.5131	−19.8439	December 02, 2015	2.9	9.5	6	51.7	0.1	0.996	0.065	51.4	3.4
MOZ4	CSF19	36.8721	−19.39	December 03, 2015	2.4	9.5	6	40.1	2	0.997	0.046	39.9	3.8
MOZ4	CSF20	39.9316	−18.4464	December 07, 2015	2.4	11.5	6	39.6	6.6	0.871	0.076	34.5	8.8

4. Heat flow prediction: method and results

4.1. Similarity method

In order to extrapolate heat flow data in poorly covered areas, Goutorbe et al. (2011) proposed an innovative approach using a large set of empirical proxies. This method is based on the evaluation, at each location of a grid, of the number of similarities N_{sim} with several heat flow proxies at all other locations of the grid where surface heat flow is known. Two cells are similar if they belong to the same class (e.g., Paleozoic), the same range (e.g., elevation between 1000 and 1200 m), or the same class of distance to a specific feature (e.g., distance to transform zones) below a threshold value (less than 500 km). Indeed, heat flow cannot be affected by a given feature over an infinite distance and this distance is fixed at 500 km (Lucazeau, 2019). Each additional similarity increases the weight w_i in the collection of heat flows by a factor K, whose optimal values were estimated to ~10 (Goutorbe et al., 2011).

$$w_i = K^{N_{sim}}$$

Classical statistics (mean Q and standard deviation σ_Q) provide estimates of the average value Q and its uncertainty σ_Q from the collection of heat flow.

$$\overline{Q} = \frac{\sum_i w_i Q_i}{\sum_i w_i}$$

Derived from the predicted heat flow value ($\overline{Q}$) and the standard deviation (σ_Q), an indicator of the prediction quality (Qual) is defined by four categories, from the best quality (A) to the less good (D). This indicator is calculated as follow:

$$\text{Qual} = \frac{\sigma_Q}{\overline{Q}}$$

The four categories are: (1) grade A with Qual $\leq$ 10%; (2) grade B with Qual $\leq$ 20%; (3) grade C with Qual $\leq$ 30%; and (4) grade D with Qual >30%.

All the detail about the method is provided in Goutorbe et al. (2011). Recently, Lucazeau (2019) realized a resolution improvement on the global prediction, from 1° × 1° to 0.5° × 0.5°, but also on the number of the available proxies used in the calculation (24–50) and on the optimum number of proxies needed for a prediction. The predictability of the similarity method depends strongly on the number and the quality of proxies. The greater the number of proxies, the smaller the misfit between heat flow data q_{prox} and predicted heat flow q_{pred}.

$$misfit = \sqrt{\frac{\sum \left(q_{prox} - q_{pred}\right)^2}{N_{prox}}}$$

Still, too many proxies can produce artefacts where no heat flow data exists, especially if the quality of these proxies is not good. Therefore, there is a trade-off between an acceptable misfit and a more likely prediction. The optimized set used in the predictions is around 14 proxies, reaching a misfit of less than 6 mW/m^2 and avoiding artefacts. For further details Lucazeau (2019).

We apply the optimized global prediction discussed above on a 0.5° × 0.5° resolution but also realize a novel local prediction on a higher resolution (0.1° × 0.1° grid) including several proxies only available in

the Mozambique channel. The complete list of the available proxies is detailed in Table S4.

4.2. Proxies used for the predictions

For the global prediction, we obtained an optimized calculation with 15 proxies considered as the best combination for an optimized prediction (Table 3). The selected best proxies are related to the age of the continental and oceanic crusts, the free air gravity anomalies, the curie point depth, the upper mantle shear velocities, the mantle density anomalies, the crustal thickness, ruggedness of the seafloor topography, the whole mantle anisotropy, the Bally-Snell classification of basins, the distances to the orogens, to the extended crust, to the continental/oceanic boundaries, to the Cenozoic rifts, to the transform zones and to the Archean and Proterozoic orogens.

The optimized procedure being unavailable for the local heat flow calculations, we selected 14 proxies sometimes different from the global heat flow predictions (Fig. 3). Some of the selected proxies show an improved resolution and/or with local constraints: the sediment thickness, the bathymetry-topography, the continental-oceanic boundaries and the distance to the transform zones. One has been specifically designed for local predictions, around the Mozambique channel, the genetic domains. The proxy selection was guided by the diversity of the constraints: (1) the data type (geological vs geophysical), (2) the scale of the proxy (surface/basin vs crust vs mantle) and (3) the category of the proxy (continuous vs class vs "distance to"). Most proxies have a resolution equal or higher than our prediction grid (0.1° × 0.1°), but one has only the resolution of our global prediction grid (0.5° × 0.5°: the whole mantle anisotropy).

All the selected proxies are presented in Table 3 and Fig. 3, see the Supplementary material (Tables S5–S8) for the class explanations.

4.3. Results: global and local predictions

4.3.1. The global prediction (0.5° × 0.5° grid)

For the heat flow prediction with the similarity method where we use only globally described proxies, a grid resolution of 0.5° × 0.5° is applied (as by Lucazeau, 2019). Our proxy optimization procedure resulted in a tradeoff of 15 best proxies, summarized in Table 3, while the heat flow predictive map is presented in Fig. 4a. The misfit between the existing and the predicted heat flow values is 2.1 mW/m^2. The prediction mapping shows a good quality, with almost 83 % of good and very good quality of prediction. As a reminder, the misfit corresponds to the difference between the observed and the predicted heat flow values where a heat flow data is available, depending on the number of proxies used in the calculation.

Here, we focused the description of the heat flow prediction on the Mozambique Channel area (Fig. 4b and c). In most of the studied area, the predicted heat flow values do not show high variations and are relatively low (35–55 mW/m^2) expected for old oceanic crust (Fig. 4b). The inland part of the African plate is characterized by a relative homogeneous heat flow prediction, with however moderate to high values in the northern part of Mozambique and in the southern part of Tanzania. Even if the high value predictions from the Madagascar island seem to be similar to its conjugate margin, i.e., the African plate north to the 10°S (Roche and Ringenbach, 2022), the island shows in its overall more contrasted heat flow predictions (Fig. 4b). Concerning the offshore predictions, the heat flow background is mainly low (<60 mW/m^2) while moderate heat flow anomalies are observed close to the Tanzanian coast, as well as close to the central coast of Madagascar island (Fig. 4b). The offshore moderate anomaly, close to the Tanzanian coast seems to draw a N–S orientation, while the heat flow predictions along the coast from Beira to Mogincual seem to follow a NE-SW orientation, the same orientation as the coastline. It is interesting to note that the heat flow prediction is, generally, lower in the southern part of the Mozambique Channel than in the northern part.

Table 3
Synthesis of the 14 proxies used into the global heat flow calculation (0.5° × 0.5° grid).

	Proxies used in the calculation	Misfit (mW/m^2)
1	Age of the oceanic and continental crust – DIST	47.9
2	All orogens – DIST	43.1
3	Curie point depth – CLASS	35.5
4	Free air anomaly – CLASS	28.9
5	Upper mantle shear velocities – CONT	21.7
6	Mantle density anomaly – CONT	13.1
7	Crustal thickness – CONT	8.2
8	Seafloor topography ruggedness – CONT	5.9
9	Whole mantle anisotropy – CLASS	4.6
10	Cenozoic rifting – DIST	3.6
11	Basin type (Bally-Snell) – CLASS	3.1
12	Continent-Ocean boundary – DIST	2.6
13	Extended crust – DIST	2.4
14	Archean & Proterozoic orogens – DIST	2.3
15	Oceanic tectonic structures - DIST	2.1

4.3.2. The local prediction (0.1° × 0.1° grid)

Using in our local study area a set of proxies available on a higher resolution (0.1° × 0.1°), we made a heat flow prediction on this increased grid resolution. The heat flow prediction mapping using 14 proxies is presented in Fig. 5. In the overall studied area, the predicted heat flow values are relatively low. The heat flow minimum is 21 mW/m^2, the heat flow maximum is 235 mW/m^2 and the heat flow mean is 59 mW/m^2 with a standard deviation of 22 mW/m^2. The misfit between the existing and the predicted heat flow values is 2.28 mW/m^2.

The prediction mapping shows good quality, with almost 70 % of good and very good quality of prediction (Fig. 5). The lowest quality (12 %) is mainly associated with the high heat flow prediction anomalies, where the variability of heat flow data is increased.

Tanzania shows a heterogeneous heat flow prediction, with areas of quite low heat flow values (Fig. 5). Close to the coastline at the frontier between Tanzania and Mozambique, a high heat flow zone, located onshore, shows an overall N–S orientation. This area is quite homogeneous with heat flow values ranging from 100 to 105.6 mW/m^2 reaching in one place 160 mW/m^2. The southern part of Mozambique, down to Malawi, is characterized by homogeneously intermediate heat flow values, ranging between 45 and 65 mW/m^2 (Fig. 5). The northern part of Mozambique is more heterogeneous with values as low as 26 mW/m^2 and as high as 144 mW/m^2. A homogeneous high heat flow prediction zone is observed, located between the Mogincual and the Pebane transects and showing a NE-SW orientation, with values ranging from 120 to 132 mW/m^2. The global heat flow of Madagascar Island is quite homogeneous and slightly higher than the mean heat flow of the African part, ranging from 50 to 80 mW/m^2, with locally values from 32 mW/m^2 to 154 mW/m^2 (Fig. 5). All the offshore periphery of Madagascar Island, except the northern coast with low heat flow values between 37 and 55 mW/m^2, is characterized by intermediate and moderately high heat flow values reaching 131 mW/m^2, but mostly comprised between 55 and 80 mW/m^2.

Concerning the heat flow prediction in the offshore domain, it appears heterogeneous with areas showing low values around 26 mW/m^2 while the highest values reach the maximum, of 235 mW/m^2 (Fig. 5). A background heat flow prediction can be proposed, with values around 50–65 mW/m^2. In addition to a such 50–65 mW/m^2 background, several anomalies can be observed highlighting either low heat flow values or very high heat flow predictions. Two major areas show very high predicted heat flow in the central part of the South Mozambique Basin and the other between the Comoros archipelago and Madagascar Island (Fig. 5). The one in the south Mozambique Basin and NE-SW oriented, with values ranging from 68 to 228 mW/m^2. The second one draws a more disrupted shape but highlights a double orientation, one NE-SW and the other NW-SE. The heat flow predictions in that place show values from around 70 up to 235 mW/m^2. Close to the Tanzania coast in

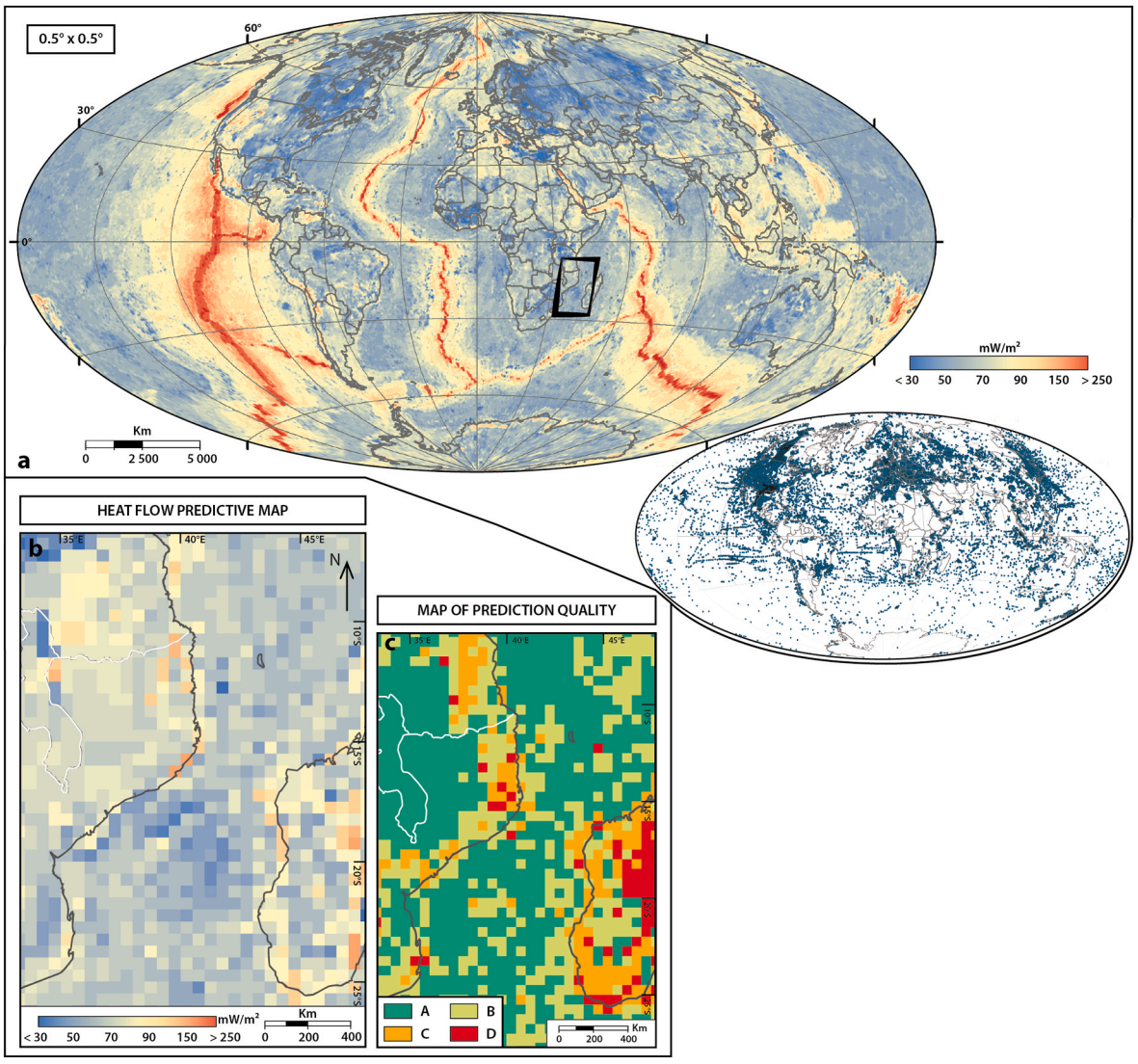

Fig. 4. Predictive heat flow map. (a) Global prediction of the heat flow according to a 0.5° × 0.5° grid. All the available heat flow data from the NGHF database (Lucazeau, 2019) with a quality code of A to C are presented with a 2021 update. (b) Zoom on the Mozambique Channel area. (c) Quality map of the predicted heat flow map.

the northern part of the studied area and shows a N–S orientation. Here, heat flow values are quite homogeneous and comprised between 65 and 86 mW/m^2. In contrast, several low heat flow anomalies are observed in different places (Fig. 5). One is located in the northeastern quarter of the studied area and shows heat flow predictions mainly comprised between 30 and 50 mW/m^2. Down to the south, surrounding the Comoros archipelago in the north, east and south, a quite homogeneous area shows heat flow values comprised between 32 and 49 mW/m^2. The southern part of this anomaly is NE-SW oriented. South to the Comoros archipelago and along the northern coast of Madagascar Island, a thin strip, highlighting a NE-SW orientation, shows heat flow predictions around 37–47 mW/m^2. Located between the Comoros archipelago and Africa, a low heat flow prediction zone is observed with a N–S orientation and values mostly comprised between 25.5 and 35 mW/m^2 (Fig. 5). The central part of the Mozambique Basin shows quite low heat flow predictions either oriented NE-SW or N–S (Fig. 5). One oriented along a NE-SW direction highlights homogeneous predictions around 45–48 mW/m^2. This anomaly is located directly down to the south of the Mozambique coast in the Mogincual and Pebane transects area. Along this anomaly in the east side, lower heat flow predictions are observed with values around 31–35 mW/m^2 and showing a N–S orientation. Again, down to the south, a circular anomaly is observed showing heat flow values comprised from 26 up to 50 mW/m^2. Toward the west, a curved anomaly is observed showing an orientation from NE-SW (in the west part) to N–S (in the east part) direction. Here, heat flow predictions are comprised between 32 and 42 mW/m^2.

4.4. *Comparison between the 0.5° × 0.5° to the 0.1° × 0.1° resolution maps*

Apart from the resolution improvement, several major points can be highlighted in the comparison between the 0.5° × 0.5° and the 0.1° × 0.1° predictive maps (Figs. 4 and 5). However, it is important to remind that the predictive maps are not based on the same proxies (Table 3 and Fig. 3). Indeed, the global predictive map, with the 0.5° × 0.5° resolution, integrates the identified "best proxies" combination according to the Lucazeau (2019) methodology, i.e. the optimized procedure (*for more details please refer to* Lucazeau (2019) *or to section 4.1. Similarity method*).

Overall, the predicted heat flow in the Mozambique Channel area is quite low for both the 0.5° and 0.1° resolutions. On both maps, the predicted background heat flow is around 60 mW/m^2 (Figs. 4 and 5).

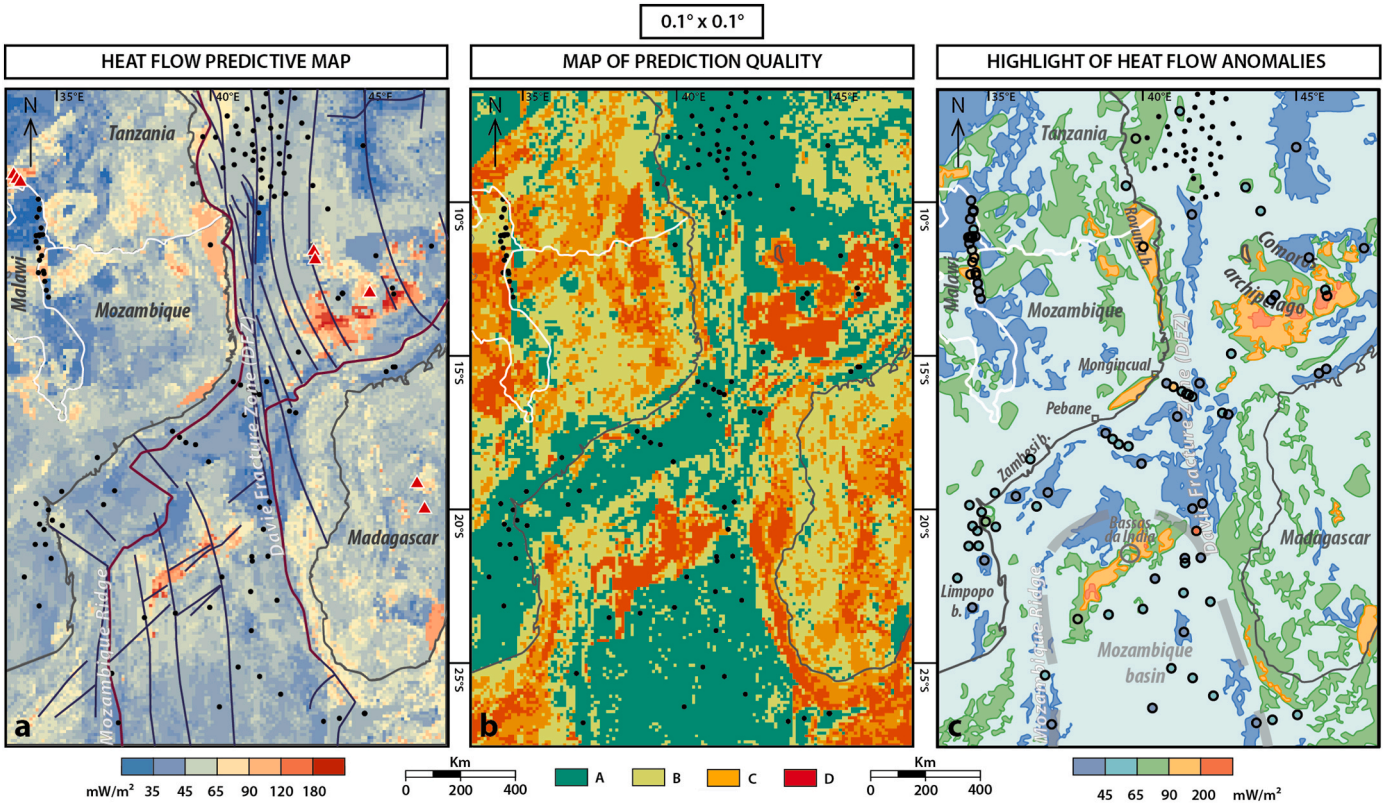

Fig. 5. Predictive heat flow map for the Mozambique Channel area. (a) Heat flow predictive map according to a 0.1° × 0.1° grid with the location of the heat flow data used in the calculation by black dots as well as the major tectonic features in dark blue lines, the Continent-Ocean Boundaries in purple line and the Holocene volcanoes in red triangles. (b) Quality map of the heat flow prediction with the location of the used heat flow data. The four quality grades are referring to the quality of the prediction, with the best quality (grade A) to the less good (grade D). (c) Simplified predictive map highlighting the main anomalies, either high or low where heat flow data are either located by black dots or showing the value of the determination. The colour scale bar is valid for both the simplified predictive map and the heat flow values.

This is most evident on global predictive map because extreme heat flow anomalies are absent on this map (Fig. 4). However, several heat flow anomalies are observed in both the 0.5° and 0.1° resolution maps. A high heat flow anomaly is observed in Mozambique between the Mogincual and Pebane transects. High heat flow values are predicted at the frontier between Tanzania and Mozambique, close to the coast, however, the shape and the extend are not the same. The western coast of Madagascar Island highlights moderate heat flow predictions in both cases, but the shape and extent are different.

The major difference is the high heat flow predictions located in the offshore part of the Mozambique Channel not observed on the 0.5° resolution map (Figs. 4 and 5). Indeed, the offshore part of the Mozambique Channel area is quite homogeneous with low heat flow values in the 0.5° resolution case. The Madagascar Island shows a quite opposite background, because the 0.5° resolution predictive map provides low heat flow values while the 0.1° resolution predictive map highlights moderate high heat flow values.

5. Discussion

5.1. Heat flow data versus regional prediction

The empiric nature of the similarity method limits their accuracy, since the outcome is strongly depending on the quality of the heat flow examples and guiding data sets; biased heat flow data will also be extrapolated (Goutorbe et al., 2011). The strong weight of each additional similarity will intrinsically also lead to a close prediction at sites with a heat flow example.

Isolated measured heat flow anomalies are clearly translated in predicted zones of low or high heat flow (Fig. 5). The extent and shape of these predicted anomalies are highly variable and depend on the surrounding heat flow examples and the different proxy layers. Two examples of isolated high heat flow stations that result in regional zones of elevated heat flow can be observed around the Bassas da India zone and near the Comoros Archipelago (Fig. 5c). Where the predicted heat flow near Bassas da India can be linked to the active faults in the Mozambique basin (Deville et al., 2018), the large predicted anomaly south of the Comoros Archipelago might be in part an artefact as Rolandone et al. (2022) interpreted the measured heat flow high a local effect of the active underwater volcano Fani Maoré east of Mayotte. On land heat flow data are very sparse and mainly located in and around lake Malawi and in the Limpopo and Zambesi basins (Fig. 5). In the Rovuma basin one isolated heat flow station on land and other offshore result in distinctive predictive regimes for both domains (Fig. 5c). The danger of the extrapolation of a biased heat flow example has to be considered in particular for such isolated stations. We see, however, that similar heat flow calculations are also predicted close to Pebane and Mogincual localities, or in the southern part of the Madagascar Island (Fig. 5c). We also note that our prediction for the offshore heat flow is in good agreement with the expected values of heat flow in the plate cooling model (Stein and Stein, 1992), with an overall small heat flow increase towards younger oceanic crust (Figs. 3 and 5). This also point out that overall our data is in good agreement with the heat flow from the oceanic plate model.

5.2. Correlation of predicted trends and proxies

Our method based on multi-proxies does not allow to evaluate directly the predictive power of one specific proxy. The impact of each proxy on the heat flow calculation can not be quantitatively expressed. A possible way to identify a relationship between proxy and prediction is to observe similarities on regional trends. These correlations are not straight forward as the continuous and "distance to" proxies are often resulting in smoothed predictions in space.

5.2.1. N–S to NE-SW oriented anomalies

In the detailed presentation of the local prediction, most heat flow anomalies highlight a specific orientation, i.e., N–S and NE-SW. Such orientations seem to be mainly correlated to the major oceanic tectonic structures (Fig. 5). For example, the high heat flow anomaly located in the Mozambique Basin is defined by the NE-SW orientation of active faults (Deville et al., 2018). Another example of the relationship between heat flow anomalies and tectonic structures is the DFZ characterized by low heat flow predictions and showing a N–S orientation (Fig. 5). The high heat flow anomaly located at the frontier between Tanzania and Mozambique, close to the coastline, also shows a N–S to NNW-SSE orientation that could be related to the DFZ orientation, which marks the oriental boundary of the anomaly. In addition, the DFZ can be followed down to the south drawing a limit between low and high heat flow predictions. In that direction, The DFZ mark the oriental boundary of the oceanic domain and by the way of the Mozambique Basin, with low heat flow predictions in the west side while the eastern part is characterized by higher heat flow predictions (Fig. 5). The other Mozambique Basin boundary, the western one, is also associated with a fracture zone, i.e., the Mozambique Fracture Zone (MFZ). As the DFZ, this fracture system draws the limit between the Mozambique Basin and the African continental domain. However, the difference between the predictions on each side of the MFZ is less marked than around the DFZ.

5.2.2. Heat flow anomalies, oceanic tectonic structures and fluid circulations

It appears that most of the N–S oriented anomalies show low heat flow predictions while the NE-SW oriented anomalies highlight high heat flow predictions (Fig. 5). The most representative offshore low heat flow prediction is located in the northwestern part of the Mozambique Channel and in the northern part of the DFZ (Fig. 5). In that place, heat flow predictions are lower than 45 mW/m^2 (Fig. 5). At the opposite, high heat flow predictions, higher than 90 mW/m^2 are observed in the central part of the Mozambique Basin (Fig. 5). Such a differing prediction can be related to the sealed/active state of faults and fluid circulations (Deville et al., 2018). Indeed, when faults are sealed, no fluid circulations can occur in any direction, i.e., from the ocean to the crust or out from the crust to the ocean. Concerning active faults, it is more complicated because of the direction of the fluid circulations. If seawater comes into the crust or the exhumed mantle through faults, then cold water is involved, being responsible for the cooling of the concerned area by fluid circulations and hydrothermal reactions (Grevemeyer et al., 2005). By the way, low heat flow values are predicted in that scenario. Such a direction of fluid circulations can be associated with charging processes while the discharging modes would be linked to high heat flow predictions due to the heating of cold water into the crust (Grevemeyer et al., 2004, 2005, 2009; Liu et al., 2006).

The age of the tectonic feature can also have an impact on the dynamic of the structure and thus on fluid circulations. Even if it is one of the most reactivated tectonic features in the Mozambique Channel, the DFZ started its onset ~166 Ma and is considered as an extinct transform system since the Middle Cretaceous (Deville et al., 2018; Roche and Ringenbach, 2022), as well as the Mozambique Fracture Zone (König and Jokat, 2010; Roche et al., 2021, 2022). While main of the NE-SW oriented structures are present-day active and thus affected by fluid circulations and hydrothermal reactions (Deville et al., 2018).

5.2.3. Heat flow anomalies, Holocene volcanoes and hydrothermal activity

Recent volcanism is usually associated with high heat flow anomalies. Heat flow data near recent volcanism in the study area range from <50 mW/m^2 to >200 mW/m^2 (Prol-Ledesma and Morán-Zenteno, 2019). However, it appears that the highest heat flow values are observed close to hydrothermal manifestations associated with active volcanism and sometimes with active faults (Prol-Ledesma and Morán-Zenteno, 2019). Another study provided extremely high heat flow data around 900 mW/m^2 close to a recent volcanic structure (less than 100 000 yr) which is explained by magma cooling (Lucazeau et al., 2009). Logically, the volcanism would impact the heat flow calculations predicting moderate to high anomalies. Indeed, this type of impact is not surprising because Holocene volcanoes are often associated with high heat flow, high temperatures but also hot fluid circulations, and magma cooling due to their current activity (Lucazeau et al., 2009; Nagao and Uyeda, 1995; Prol-Ledesma and Morán-Zenteno, 2019). Such a scenario is observed in the studied area where the high heat flow anomaly located between the Comoros archipelago and Madagascar Island is shown (Fig. 5; Berthod et al., 2022; Courgeon et al., 2016).

5.2.4. Heat flow anomalies and deep seated proxies

From the deep seated proxies, such as mantle density anomalies, tomography anomaly or Curie point depth, the relation to the surface heat flow is particularly well described in literature for the latter proxies (Bilim et al., 2016; Li et al., 2017; Saleh et al., 2013). For our heat flow prediction, we observe that this is not everywhere the case in our study area. For example, the high heat flow anomalies predicted between the Comoros archipelago and the Madagascar island should be linked to a shallow Curie point depth. This is not so clear, because in this area, the Curie point depth is around 20 km, i.e., a meaning depth (Figs. 3 and 5). But shapes of both the heat flow prediction and the Curie point depth highlight similarities. Another shape similarity is with the sediment thickness proxy (Figs. 3 and 5). In this area, an association of an important thickness of sediments and a mean Curie point depth could explain such high heat flow calculations. But this hypothesis is valid only if around the Curie point depths are quite constant when sediment thickness is thinner and associated to lower heat flow predictions. However, very shallow Curie point depths are observed in the Comoros Archipelago without so high heat flow values (Figs. 3 and 5). A possible explanation could come from the heat flow data used in the predictive calculation. Indeed, in that place, new heat flow data were acquired showing very high values (Fig. 2). Such high values associated with the local geological and geophysical characteristics could explain such a prediction, i.e., high heat flow anomaly (Figs. 3 and 5). This would imply that the high heat flow data share with high heat flow predictions common geological or geophysical characteristics, i.e., a combination of proxies and not exclusively the Curie point depth proxy.

Located on the Comoros archipelago, the medium to high heat flow predictions show a specific shape which can correspond to shapes observed in the genetic domain and/or free air anomaly proxies (Figs. 3 and 5). Regarding the genetic domain proxy, the predicted heat flow anomaly is consistent with the crust nature at that place, which is volcanic, i.e., resulting to recent volcanic activity. This specific shape is also correlated with the free air anomaly proxy, highlighting values consistent with the nature of the crust. This volcanic archipelago is also synonymous of strong differential in the bathymetry (Figs. 2 and 3). All together, these elements explain the heat flow anomaly prediction at the Comoros archipelago place (Figs. 2, 3 and 5; Choi et al., 2013; Li and Song, 2012; Lillis et al., 2015).

5.3. Comparison to recent heat flow studies

Recent works focused on the spatial variation of the heat flow and the understanding of the anomaly location at several scales, from the African plate to the Malawi country scale, but only deal with terrestrial data and/or estimations (Didas et al., 2022; Gomes et al., 2021; Jones,

2020; Macgregor, 2020). It appears that heat flow data and predictions are highly variable depending on the studies. Differences in these results can come from calculation methods, (1) punctual calculations using thermal gradient derived from deep well measurements and lithology-based thermal conductivities (Macgregor, 2020) and (2) predictive map compiling calculations based on gravity data (Didas et al., 2022). Based on a similar approach, Gomes et al. (2021) used geothermal data with a thermal correction using an equation from Hamza (1982). Whatever the calculation method, they are all based on one main element, i.e., deep well data, gravity data or geothermal data. Even if the heat flow calculation appears quite simple, many parameters can affect it or at least inferred a link with it, like the sedimentation rates (Hutchison, 1985; Theissen and Rüpke, 2010), the nature of the continent/ocean crust (Chapman and Rybach, 1985; Mareschal and Jaupart, 2013; Stein and Stein, 1992), or the Curie point depth (Li et al., 2017) or again, the lithosphere-asthenosphere boundary structure (Richards et al., 2018) and the mantle shear wave anomalies (Artemieva, 2006; Pollack et al., 1993). Locally or in specific cases, one of these elements can be predominant from others allowing such a one-element approach for heat flow predictions. However, the complexity of the geothermal gradient or the surface heat flow manifestations imply difficulties to accurately predict heat flow where no data are available, especially for global predictions. This is why a multi-proxy approach could be a way to better predict both regional trends and anomalies like in the northern part of the Malawi or between the Comoros archipelago and Madagascar Island. Indeed, the heat flow estimations can be affected by local effects or local anomalies, like fluid circulations, especially with the use of only deep wells data. At the opposite, the use of only one regional element for calculations, like the Curie point depth or the gravimetry data, does not allow to proceed to a very precise prediction, taking into account of very punctual effects or superficial anomalies (Artemieva, 2006; Didas et al., 2022; Gomes et al., 2021; Li et al., 2017).

5.4. Resolution, limitations and development perspectives

We showed that the successful application of the similarity method for extrapolating surface heat flow data, guided by a set of proxies, at a higher resolution than its initial application on a $1^\circ \times 1^\circ$ grid (Goutorbe et al., 2011). On a global scale, the prediction was refined to a resolution of $0.5^\circ \times 0.5^\circ$ by Lucazeau (2019) and further optimized in this study. Additionally, we extended the application of the prediction method to a regional area around the Mozambique Channel with an increased resolution of $0.1^\circ \times 0.1^\circ$. Different local heat flow anomalies are outlined on a kilometric scale that helps to better constrain the thermal history in individual sedimentary basins and the hosting petroleum systems. The statistics of the predicted heat flow also exhibit a good predictability and low RMS error on this heightened resolution. However, the empiric approach limits the outcome to the quality of the heat flow examples and guiding data sets. Within the study area, it is crucial that most of the proxies possess a resolution equal to or higher than the prediction grid. While specific proxies exclusive to the study area can be incorporated, there remains a need to develop proxy optimization for local predictions. Furthermore, the establishment of a blind test procedure will facilitate a more robust evaluation of the predictability of the similarity method on this higher resolution.

6. Conclusion

Using the similarity method approach completed by local proxies and updated by new heat flow data, a predicted map of the heat flow around the Mozambique Channel can be proposed. This extrapolation based on a $0.1^\circ \times 0.1^\circ$ grid allows a precise prediction with good predictability on 70% of pixels and an RMS error lower than 2.3 mW/m^2. The selected proxies used in the heat flow calculation are related to local geology and geophysical characteristics, either at several scales (surface, basin, crustal or lithosphere scale).

The predictive map highlights an overall low heat flow background, around 50 mW/m^2, which agrees with both the new heat flow data and the age of the oceanic crust. Regional N–S and NE-SW orientations are associated with heat flow anomalies and are suspected to be related to the main tectonic structures. The first one shows low heat flow predictions, i.e., <50 mW/m^2, while the second highlights very high heat flow values, i.e., >85 mW/m^2. In addition to the age of the crust and the tectonic features, several other proxies have a suspected impact on the heat flow predictions, i.e., the free air anomaly classification proxy, the Bouguer anomaly classification proxy, the Holocene volcanoes, the Curie point depth classification proxy, or again, the genetic domains proxy. Logically, recent active volcanoes are associated with high heat flow predictions, while the other proxies can either be associated with high or low heat flow predictions.

CRediT authorship contribution statement

Eloïse Bessière: Writing – review & editing, Writing – original draft, Validation, Methodology, Investigation, Formal analysis, Data curation. **Jeffrey Poort:** Writing – review & editing, Writing – original draft, Validation, Supervision, Methodology, Data curation. **Tristan Cornu:** Writing – review & editing, Supervision. **Sylvie Leroy:** Writing – review & editing, Data curation.

Declaration of competing interest

The authors declare the following financial interests/personal relationships which may be considered as potential competing interests: Eloise Bessiere reports financial support was provided by Sorbonne University.

Data availability

All the used data in this study are free or from published databases - please refer to the references in the text or to the publication of Lucazeau (2019).

Acknowledgements

All the used data in this study are free or from published databases (please refer to the references in the text or to the publication of Lucazeau (2019)), for example, the Curie point depths are from Li et al. (2017), the global sediment thickness (GlobSed) is from Straume et al. (2019), the topography and bathymetry are from GTOPO30 (DOI: 10.5066/F7DF6PQS) or GEBCO2020 (https://doi.org/10.5285/a29c5465-b138-234d-e053-6c86abc040b9). The PAMELA project (PAssive Margin Exploration Laboratories), a scientific project led by Ifremer and TotalEnergies in collaboration with Université de Bretagne Occidentale, Université Rennes 1, Sorbonne Université, CNRS and IFPEN, is thanked for the Heat Flow data from MOZ1, MOZ2 and MOZ4 cruises. This project was dedicated to improve the understanding of processes along continental margins, focused on the Gulf of Gascogne, the Corsica and the Mozambique channels. Finally, this paper benefited from efficient handling by Associate Editor, Ahmed E. Radwan, and throughtful comments from four anonymous reviewers, which clarified and expanded critical points of the original draft.

Appendix A. Supplementary data

Supplementary data to this article can be found online at https://doi.org/10.1016/j.marpetgeo.2024.106723.

References

Anderson, R.N., Langseth, M.G., Sclater, J.G., 1977. The mechanisms of heat transfer through the floor of the Indian Ocean. J. Geophys. Res. 82 (23), 3391–3409.

Artemieva, I.M., 2006. Global 1× 1 thermal model TC1 for the continental lithosphere: implications for lithosphere secular evolution. Tectonophysics 416 (1–4), 245–277.

Benfield, A.E., 1939. Terrestrial heat flow in Great Britain. Proc. Roy. Soc. Lond. Math. Phys. Sci. 173 (955), 428–450.

Berthod, C., Bachèlery, P., Jorry, S.J., Pitel-Roudaut, M., Ruffet, G., Revillon, S., Courgeon, S., Doucelance, R., 2022. First characterization of the volcanism in the southern Mozambique Channel: Geomorphological and structural analyses. Mar. Geol. 445, 106755.

Bilim, F., Akay, T., Aydemir, A., Kosaroglu, S., 2016. Curie point depth, heat-flow and radiogenic heat production deduced from the spectral analysis of the aeromagnetic data for geothermal investigation on the Menderes Massif and the Aegean Region, western Turkey. Geothermics 60, 44–57.

Bingen, B., Jacobs, J., Viola, G., Henderson, I.H.C., Skår, Ø., Boyd, R., Thomas, R.J., Solli, A., Key, R.M., Daudi, E.X.F., 2009. Geochronology of the Precambrian crust in the Mozambique belt in NE Mozambique, and implications for Gondwana assembly. Precambrian Res. 170 (3–4), 231–255.

Bonvalot, S., Balmino, G., Briais, A., Kuhn, M., Peyrefitte, A., Vales, N., Biancale, R., Gabalda, G., Reinquin, F., Sarrailh, M., 2012. World Gravity Map. Commission for the Geological Map of the World. BGI-CGMW-CNES-IRD, Paris. http://doi.org/10.81168/bgi.23.

Bullard, E.C., 1939. Heat flow in South Africa. Proc. Roy. Soc. Lond. Math. Phys. Sci. 173 (955), 474–502.

Bullard, E.C., 1954. The flow of heat through the floor of the Atlantic Ocean. Proc. Roy. Soc. Lond. Math. Phys. Sci. 222 (1150), 408–429.

Castaing, C., 1991. Post-Pan-African tectonic evolution of South Malawi in relation to the Karroo and recent East African rift systems. Tectonophysics 191 (1–2), 55–73.

Catuneanu, O., Wopfner, H., Eriksson, P.G., Cairncross, B., Rubidge, B.S., Smith, R.M.H., Hancox, P.J., 2005. The Karoo basins of south-central Africa. J. Afr. Earth Sci. 43 (1–3), 211–253.

Cawood, P.A., Buchan, C., 2007. Linking accretionary orogenesis with supercontinent assembly. Earth Sci. Rev. 82 (3–4), 217–256.

Chapman, D.S., Rybach, L., 1985. Heat flow anomalies and their interpretation. J. Geodyn. 4 (1–4), 3–37.

Choi, S., Oh, C.W., Götze, H.J., 2013. Three-dimensional density modeling of the EGM2008 gravity field over the Mount Paekdu volcanic area. J. Geophys. Res. Solid Earth 118 (7), 3820–3836.

Coffin, M.F., Rabinowitz, P.D., 1987. Reconstruction of Madagascar and Africa: evidence from the Davie fracture zone and western Somali basin. J. Geophys. Res. Solid Earth 92 (B9), 9385–9406.

Collins, A.S., Pisarevsky, S.A., 2005. Amalgamating eastern Gondwana: the evolution of the circum-Indian orogens. Earth Sci. Rev. 71 (3–4), 229–270.

Courgeon, S., Jorry, S.J., Camoin, G.F., BouDagher-Fadel, M.K., Jouet, G., Révillon, S., Bachèlery, P., Pelleter, E., Borgomano, J., Poli, E., Droxler, A.W., 2016. Growth and demise of Cenozoic isolated carbonate platforms: new insights from the Mozambique Channel seamounts (SW Indian Ocean). Mar. Geol. 380, 90–105.

Cox, K.G., 1992. Karoo igneous activity, and the early stages of the break-up of Gondwanaland. Geological Society, London, Special Publications 68 (1), 137–148.

Daly, M.C., Chorowicz, J., Fairhead, J.D., 1989. Rift basin evolution in Africa: the influence of reactivated steep basement shear zones. Geological Society, London, Special Publications 44 (1), 309–334.

Daszinnies, M.C., Jacobs, J., Wartho, J.A., Grantham, G.H., 2009. Post Pan-African thermo-tectonic evolution of the north Mozambican basement and its implication for the Gondwana rifting. Inferences from 40Ar/39Ar hornblende, biotite and titanite fission-track dating. Geological Society, London, Special Publications 324 (1), 261–286.

Davies, G.F., 1989. Mantle convection model with a dynamic plate: topography, heat flow and gravity anomalies. Geophys. J. Int. 98 (3), 461–464.

Davies, J.H., 2013. Global map of solid Earth surface heat flow. G-cubed 14 (10), 4608–4622.

Deville, E., Marsset, T., Courgeon, S., Jatiault, R., Ponte, J.P., Thereau, E., Jouet, G., Jorry, S.J., Droz, L., 2018. Active fault system across the oceanic lithosphere of the Mozambique Channel: implications for the Nubia–Somalia southern plate boundary. Earth Planet Sci. Lett. 502, 210–220.

Didas, M.M., Armadillo, E., Hersir, G.P., Cumming, W., Rizzello, D., 2022. Regional thermal anomalies derived from magnetic spectral analysis and 3D gravity inversion: implications for potential geothermal sites in Tanzania. Geothermics 103, 102431.

Ebinger, C.J., Rosendahl, B.R., Reynolds, D.J., 1987. Tectonic model of the malaŵi rift, africa. Tectonophysics 141 (1–3), 215–235.

Evans, T.R., 1975. Terrestrial Heat Flow Studies in Eastern Africa and the North Sea.

Franke, D., Jokat, W., Ladage, S., Stollhofen, H., Klimke, J., Lutz, R., Mahanjane, E.S., Ehrhardt, A., Schreckenberger, B., 2015. The offshore East African Rift System: structural framework at the toe of a juvenile rift. Tectonics 34 (10), 2086–2104.

Fuchs, S., Norden, B., Artemieva, I., Chiozzi, P., Dedecek, P., Demezhko, D., Förster, A., Gola, G., Gosnold, W., Hamza, V., Harris, R., He, L., Huang, S., Kohl, T., Lee, Y., Liu, S., Podugu, N., Negrete-Aranda, R., Poort, J., Roy, S., Tanaka, A., Vakhitova, G., Verdoya, M., 2021. The Global Heat Flow Database. Release, 2021.

Furlong, K.P., Spakman, W., Wortel, R., 1995. Thermal structure of the continental lithosphere: constraints from seismic tomography. Tectonophysics 244 (1–3), 107–117.

Fuchs, S., Norden, B., Neumann, F., Kaul, N., Tanaka, A., Kukkonen, I.T., Pascal, C., Christiansen, R., Gola, G., Safanda, J., Espinoza-Ojeda, O.M., Marzan, I., Rybach, L., Balkan-Pazvantoglu, E., Ramalho, E.C., Dedecek, P., Negrete-Aranda, R., Balling, N., Poort, J., Wang, Y., Joeleth, A., Rajver, D., Gao, X., Liu, S., Harris, R., Richards, M., McLaren, S., Chiozzi, P., Nunn, J., Madon, M., Beardsmore, G., Funnell, R., Duerrast, H., Jennings, S., Elger, K., Pauselli, C., Verdoya, M., 2023. Quality-assurance of heat-flow data: the new structure and evaluation scheme of the IHFC Global Heat Flow Database. Tectonophysics 863. https://doi.org/10.1016/j.tecto.2023.229976.

Gaina, C., Torsvik, T.H., van Hinsbergen, D.J., Medvedev, S., Werner, S.C., Labails, C., 2013. The African Plate: a history of oceanic crust accretion and subduction since the Jurassic. Tectonophysics 604, 4–25.

Gomes, J.L., Vieira, F.P., Hamza, V.M., 2021. Reappraisal of heat flow variations in mainland Africa. Int. J. Terr. Heat Flow Appl. Geothermics 4 (1), 26–78.

Goutorbe, B., Lucazeau, F., Bonneville, A., 2008. The thermal regime of South African continental margins. Earth Planet Sci. Lett. 267 (1–2), 256–265.

Goutorbe, B., Poort, J., Lucazeau, F., Raillard, S., 2011. Global heat flow trends resolved from multiple geological and geophysical proxies. Geophys. J. Int. 187 (3), 1405–1419.

Grevemeyer, I., Villinger, H., 2001. Gas hydrate stability and the assessment of heat flow through continental margins. Geophys. J. Int. 145 (3), 647–660.

Grevemeyer, I., Kopf, A.J., Fekete, N., Kaul, N., Villinger, H.W., Heesemann, M., Wallmann, K., Spiess, V., Gennerich, H.-H., Müller, M., Weinrebe, W., 2004. Fluid flow through active mud dome Mound Culebra offshore Nicoya Peninsula, Costa Rica: evidence from heat flow surveying. Mar. Geol. 207 (1–4), 145–157.

Grevemeyer, I., Kaul, N., Diaz-Naveas, J.L., Villinger, H.W., Ranero, C.R., Reichert, C., 2005. Heat flow and bending-related faulting at subduction trenches: case studies offshore of Nicaragua and Central Chile. Earth Planet Sci. Lett. 236 (1–2), 238–248.

Grevemeyer, I., Kaul, N., Kopf, A., 2009. Heat flow anomalies in the Gulf of cadiz and off cape san vincente, Portugal. Mar. Petrol. Geol. 26 (6), 795–804.

Hamza, V.M., 1982. Thermal structure of South American continental lithosphere during Archean and Proterozoic. Revista brasileira de geaociências 12 (1–3), 149–159.

Hutchison, I., 1985. The effects of sedimentation and compaction on oceanic heat flow. Geophys. J. Int. 82 (3), 439–459.

Hyndman, R.D., Foucher, J.P., Yamano, M., Fisher, A., 1992. Deep sea bottom-simulating-reflectors: calibration of the base of the hydrate stability field as used for heat flow estimates. Earth Planet Sci. Lett. 109 (3–4), 289–301.

Ivanov, A.V., Meffre, S., Thompson, J., Corfu, F., Kamenetsky, V.S., Kamenetsky, M.B., Demonterova, E.I., 2017. Timing and genesis of the Karoo-Ferrar large igneous province: new high precision U-Pb data for Tasmania confirm short duration of the major magmatic pulse. Chem. Geol. 455, 32–43.

Jacobs, J., Thomas, R.J., 2004. Himalayan-type indenter-escape tectonics model for the southern part of the late Neoproterozoic–early Paleozoic East African–Antarctic orogen. Geology 32 (8), 721–724.

Jacobs, J., Pisarevsky, S., Thomas, R.J., Becker, T., 2008. The kalahari craton during the assembly and dispersal of rodinia. Precambrian Res. 160 (1–2), 142–158.

Jokat, W., Boebel, T., König, M., Meyer, U., 2003. Timing and geometry of early Gondwana breakup. J. Geophys. Res. Solid Earth 108 (B9).

Jones, D.J.R., 2020. A Summary of the East Africa Rift Temperature and Heat Flow Model (EARTH).

Jouet, G., Deville, E., 2015. PAMELA-MOZ04 Cruise, RV Pourquoi Pas. *Flotte océanographique Française Opérée Par l'Ifremer*. EAGE, Netherlands.

Klausen, M.B., 2009. The Lebombo monocline and associated feeder dyke swarm: diagnostic of a successful and highly volcanic rifted margin? Tectonophysics 468 (1–4), 42–62.

König, M., Jokat, W., 2010. Advanced insights into magmatism and volcanism of the Mozambique Ridge and Mozambique Basin in the view of new potential field data. Geophys. J. Int. 180 (1), 158–180.

Korenaga, J., 2008. Plate tectonics, flood basalts and the evolution of Earth's oceans. Terra. Nova 20 (6), 419–439.

Langseth Jr., M.G., Taylor, P.T., 1967. Recent heat flow measurements in the Indian Ocean. J. Geophys. Res. 72 (24), 6249–6260.

Lee, W.H., Uyeda, S., 1965. Review of heat flow data. Terrestrial heat flow 8, 87–190.

Leinweber, V.T., Klingelhoefer, F., Neben, S., Reichert, C., Aslanian, D., Matias, L., Heyde, I., Schreckenberger, B., Jokat, W., 2013. The crustal structure of the Central Mozambique continental margin—wide-angle seismic, gravity and magnetic study in the Mozambique Channel, Eastern Africa. Tectonophysics 599, 170–196.

Li, C., Song, T., 2012. Magnetic recording of the Cenozoic oceanic crustal accretion and evolution of the South China Sea basin. Chin. Sci. Bull. 57 (24), 3165–3181.

Li, C.F., Lu, Y., Wang, J., 2017. A global reference model of Curie-point depths based on EMAG2. Sci. Rep. 7 (1), 1–9.

Liu, C.S., Schnurle, P., Wang, Y., San-Hsiung, C., Song-Chuen, C., Hsiuan, T.H., 2006. Distribution and characters of gas hydrate offshore of southwestern Taiwan. TAO: Terr. Atmos. Ocean Sci. 17 (4), 615.

Lillis, R.J., Dufek, J., Kiefer, W.S., Black, B.A., Manga, M., Richardson, J.A., Bleacher, J. E., 2015. The Syrtis Major volcano, Mars: a multidisciplinary approach to interpreting its magmatic evolution and structural development. J. Geophys. Res.: Planets 120 (9), 1476–1496.

Loyd, S.J., Becker, T.W., Conrad, C.P., Lithgow-Bertelloni, C., Corsetti, F.A., 2007. Time variability in Cenozoic reconstructions of mantle heat flow: plate tectonic cycles and implications for Earth's thermal evolution. Proc. Natl. Acad. Sci. USA 104 (36), 14266–14271.

Lucazeau, F., 2019. Analysis and mapping of an updated terrestrial heat flow data set. G-cubed 20 (8), 4001–4024.

Lucazeau, F., Leroy, S., Autin, J., Bonneville, A., Goutorbe, B., Watremez, L., D'Acremont, E., Düsünur, D., Rolandone, F., Huchon, P., Bellahsen, N., Tuchais, P., 2009. Post-rift volcanism and high heat-flow at the ocean-continent transition of the eastern Gulf of Aden. Terra Nova 21 (4), 285–292.

Macgregor, D., 2018. History of the development of Permian–Cretaceous rifts in East Africa: a series of interpreted maps through time. Petrol. Geosci. 24 (1), 8–20.
Macgregor, D.S., 2020. Regional variations in geothermal gradient and heat flow across the African plate. J. Afr. Earth Sci. 171, 103950.
Mahanjane, E.S., 2012. A geotectonic history of the northern Mozambique Basin including the Beira High–a contribution for the understanding of its development. Mar. Petrol. Geol. 36 (1), 1–12.
Mareschal, J.C., Jaupart, C., 2013. Radiogenic heat production, thermal regime and evolution of continental crust. Tectonophysics 609, 524–534.
Marshall, B.V., Erickson, A.J., 1974. Heat flow and thermal conductivity measurements, leg 25, deep sea drilling project. Simpson and Schlich et al., Initial Reports of the Deep Sea Drilling Project 25, 349–355.
Martinelli, G., Dongarra, G., Jones, M.Q.W., Rodriguez, A., 1995. Geothermal features of Mozambique-Country update. Proceedings of the World Geothermal Congress 1, 251–273. Auckland, New Zealand: International Geothermal Association.
Masquelet, C., Leroy, S., Delescluse, M., Chamot-Rooke, N., Thinon, I., Lemoine, A., Franke, D., Watremez, L., Werner, P., Paquet, F., Berthod, C., Pico, V., Sauter, D., 2022. The East-Mayotte new volcano in the Comoros Archipelago: structure and timing of magmatic phases inferred from seismic reflection data. Compt. Rendus Geosci. 354 (S2), 1–15.
Melluso, L., Cucciniello, C., Petrone, C.M., Lustrino, M., Morra, V., Tiepolo, M., Vasconcelos, L., 2008. Petrology of Karoo volcanic rocks in the southern Lebombo monocline, Mozambique. J. Afr. Earth Sci. 52 (4–5), 139–151.
Moulin, M., Aslanian, D., Evain, M., Leprêtre, A., Schnurle, P., Verrier, F., Thompson, J., De Clarens, P., Leroy, S., Dias, N., PAMELA-MOZ35 Team, 2020. Gondwana breakup: messages from the north natal valley. Terra. Nova 32 (3), 205–214.
Mueller, C.O., Jokat, W., Schreckenberger, B., 2016. The crustal structure of Beira High, central Mozambique—combined investigation of wide-angle seismic and potential field data. Tectonophysics 683, 233–254.
Muffler, P., Cataldi, R., 1978. Methods for regional assessment of geothermal resources. Geothermics 7 (2–4), 53–89.
Nagao, T., Uyeda, S., 1995. Heat-flow distribution in Southeast Asia with consideration of volcanic heat. Tectonophysics 251 (1–4), 153–159.
Nyblade, A.A., Pollack, H.N., Jones, D.L., Podmore, F., Mushayandebvu, M., 1990. Terrestrial heat flow in east and southern Africa. J. Geophys. Res. Solid Earth 95 (B11), 17371–17384.
Olu, K., 2014. PAMELA-MOZ01 Cruise. L'Atalante R/V.
Pollack, H.N., Hurter, S.J., Johnson, J.R., 1993. Heat flow from the Earth's interior: analysis of the global data set. Rev. Geophys. 31 (3), 267–280.
Prol-Ledesma, R.M., Morán-Zenteno, D.J., 2019. Heat flow and geothermal provinces in Mexico. Geothermics 78, 183–200.
Reeves, C., 2014. The position of Madagascar within Gondwana and its movements during Gondwana dispersal. J. Afr. Earth Sci. 94, 45–57.
Reeves, C.V., 2018. The development of the East African margin during Jurassic and Lower Cretaceous times: a perspective from global tectonics. Petrol. Geosci. 24 (1), 41–56.
Richards, F.D., Hoggard, M.J., Cowton, L.R., White, N.J., 2018. Reassessing the thermal structure of oceanic lithosphere with revised global inventories of basement depths and heat flow measurements. J. Geophys. Res. Solid Earth 123 (10), 9136–9161.
Riedel, S., Jacobs, J., Jokat, W., 2013. Interpretation of new regional aeromagnetic data over dronning maud land (east Antarctica). Tectonophysics 585, 161–171.
Riley, T.R., Leat, P.T., Storey, B.C., Parkinson, I.J., Millar, I.L., 2003. Ultramafic lamprophyres of the Ferrar large igneous province: evidence for a HIMU mantle component. Lithos 66 (1–2), 63–76.
Riley, T.R., Jordan, T.A., Leat, P.T., Curtis, M.L., Millar, I.L., 2020. Magmatism of the Weddell Sea rift system in Antarctica: implications for the age and mechanism of rifting and early stage Gondwana breakup. Gondwana Res. 79, 185–196.
Ring, U., Kröner, A., Buchwaldt, R., Toulkeridis, T., Layer, P.W., 2002. Shear-zone patterns and eclogite-facies metamorphism in the Mozambique belt of northern Malawi, east-central Africa: implications for the assembly of Gondwana. Precambrian Res. 116 (1–2), 19–56.
Robin, C., Droz, L., 2014. PAMELA-MOZ02 Cruise. RV L'Atalante.
Roche, V., Leroy, S., Guillocheau, F., Revillon, S., Ruffet, G., Watremez, L., d'Acremont, E., Nonn, C., Vetel, W., Despinois, F., 2021. The Limpopo magma-rich transform margin, south Mozambique–2: implications for the Gondwana breakup. Tectonics 40 (12), e2021TC006914.
Roche, V., Ringenbach, J.C., 2022. The Davie Fracture Zone: a recorder of continents drifts and kinematic changes. Tectonophysics 823, 229188.
Rolandone, F., Poort, J., Masquelet, C., Leroy, S., Thinon, I., Lemoine, A., Paquet, F., 2022. Heat flow measurements in the northern Mozambique channel. Compt. Rendus Geosci. 354 (S2), 1–12.
Saleh, S., Salk, M., Pamukçu, O., 2013. Estimating Curie point depth and heat flow map for northern Red Sea rift of Egypt and its surroundings, from aeromagnetic data. Pure Appl. Geophys. 170 (5), 863–885.
Sclater, J.G., 1977. An analysis of the variation of ocean floor bathymetry and heat flow with age. J. Geophys. Res. 82, 803–827. https://doi.org/10.1029/JB082i005p00803.
Segoufin, J., 1978. Anomalies mesozoiques dans le bassin de Mozambique CR. Acad. Sci. Paris 267, 109–112.
Senkans, A., Leroy, S., d'Acremont, E., Castilla, R., Despinois, F., 2019. Polyphase rifting and break-up of the central Mozambique margin. Mar. Petrol. Geol. 100, 412–433.
Shapiro, N.M., Ritzwoller, M.H., 2004. Inferring surface heat flux distributions guided by a global seismic model: particular application to Antarctica. Earth Planet Sci. Lett. 223 (1–2), 213–224.
Stein, C.A., Stein, S., 1992. A model for the global variation in oceanic depth and heat flow with lithospheric age. Nature 359 (6391), 123–129.
Storey, B.C., 1995. The role of mantle plumes in continental breakup: case histories from Gondwanaland. Nature 377 (6547), 301–308.
Storey, M., Mahoney, J.J., Saunders, A.D., Duncan, R.A., Kelley, S.P., Coffin, M.F., 1995. Timing of hot spot—related volcanism and the breakup of Madagascar and India. Science 267 (5199), 852–855.
Straume, E.O., Gaina, C., Medvedev, S., Hochmuth, K., Gohl, K., Whittaker, J.M., Fattah, R.A., Doornenbal, J.C., Hopper, J.R., 2019. GlobSed: updated total sediment thickness in the world's oceans. G-cubed 20 (4), 1756–1772.
Theissen, S., Rüpke, L.H., 2010. Feedbacks of sedimentation on crustal heat flow: new insights from the Vøring Basin, Norwegian Sea. Basin Res. 22 (6), 976–990.
Thinon, I., Lemoine, A., Leroy, S., Paquet, F., Berthod, C., Zaragosi, S., Famin, V., Feuillet, N., Boymond, P., Masquelet, C., Mercury, N., Rusquet, A., Scalabrin, C., Van der Woerd, J., Bernard, J., Bignon, J., Clouard, V., Doubre, C., Jacques, E., Jorry, S., Rolandone, F., Chamot-Rooke, N., Delescuse, M., Franke, D., Watremez, L., Bachèlery, P., Michon, L., Sauter, D., Bujan, S., Canva, A., Dassie, E., Roche, V., Ali, S., Allaouia, A., Deplus, C., Rad, S., Sadeski, L., 2022. Volcanism and tectonics unveiled in the Comoros archipelago between africa and Madagascar. Compt. Rendus Geosci. 354 (S2), 7–34.
Vincent, E., 2016. Thermicité dans le segment central de la marge mozambicaine. Unpublished Master Thesis, University of Lorraine.
Von Herzen, R., Maxwell, A.E., 1959. The measurement of thermal conductivity of deep-sea sediments by a needle-probe method. J. Geophys. Res. 64 (10), 1557–1563.
Von Herzen, R.P., Langseth, M.G., 1965. "Present status of oceanic heat flow measurements. Phys. Chem. Earth 6, 365–407.
Von Herzen, R.P., Vacquier, V., 1967. Terrestrial heat flow in lake Malawi, Africa. J. Geophys. Res. 72, 4221–4226, 16.
Watkeys, M.K., 2002. Development of the Lebombo rifted volcanic margin of southeast Africa. In: Menzies, M.A. (Ed.), Volcanic Rifted Margin, vol. 362. Spec. Pap. Geol. Soc. Am., pp. 29–48 et al.
Watremez, L., Leroy, S., d'Acremont, E., Roche, V., Evain, M., Leprêtre, A., Verrier, F., Aslanian, D., Dias, N., Afilhado, A., Schnürle, P., Castilla, R., Despinois, F., Moulin, M., 2021. The Limpopo magma-rich transform margin, south Mozambique: 1. Insights from deep-structure seismic imaging. Tectonics 40 (12), e2021TC006915.
Yamano, M., Uyeda, S., Aoki, Y., Shipley, T.H., 1982. Estimates of heat flow derived from gas hydrates. Geology 10 (7), 339–343.